

## References and Notes

1. T. P. Yoon, E. N. Jacobsen, *Science* **299**, 1691–1693 (2003).
2. B. List, J. W. Yang, *Science* **313**, 1584–1586 (2006).
3. D. W. C. MacMillan, *Nature* **455**, 304–308 (2008).
4. M. Benaglia, A. Puglisi, F. Cozzi, *Chem. Rev.* **103**, 3401–3430 (2003).
5. F. Cozzi, *Adv. Synth. Catal.* **348**, 1367–1390 (2006).
6. T. E. Kristensen, T. Hansen, *Eur. J. Org. Chem.* **2010**, 3179–3204 (2010).
7. B. Merrifield, “Nobel lecture: Solid phase synthesis” (Nobel Foundation, Stockholm, 1984); available online at [www.nobelprize.org/nobel\\_prizes/chemistry/laureates/1984/merrifield-lecture.html](http://www.nobelprize.org/nobel_prizes/chemistry/laureates/1984/merrifield-lecture.html).
8. W. H. Carothers, U.S. Patent 2,130,523 (1938).
9. L. B. Hu *et al.*, *Nano Lett.* **10**, 708–714 (2010).
10. M. Pasta, F. La Mantia, L. B. Hu, H. D. Deshazer, Y. Cui, *Nano Res.* **3**, 452–458 (2010).
11. G. H. Yu *et al.*, *Nano Lett.* **11**, 2905–2911 (2011).
12. M. D. Lima *et al.*, *Science* **331**, 51–55 (2011).
13. G. Bredig, F. Gerstner, H. Lang, *Biochem. Z.* **282**, 88 (1935).
14. S. Q. Wang *et al.*, *J. Mol. Catal. Chem.* **264**, 60–65 (2007).
15. D. Praschak, T. Bahners, E. Schollmeyer, *Appl. Phys. A* **66**, 69–75 (1998).
16. S. L. Gao *et al.*, *Appl. Phys. B* **81**, 681–690 (2005).
17. K. Opwis, D. Knittel, E. Schollmeyer, *Biotechnol. J.* **2**, 347–352 (2007).
18. C. Decker, *Polym. Int.* **51**, 1141–1150 (2002).
19. A. Sakakura, K. Kawajiri, T. Ohkubo, Y. Kosugi, K. Ishihara, *J. Am. Chem. Soc.* **129**, 14775–14779 (2007).
20. M. North, R. Pasquale, C. Young, *Green Chem.* **12**, 1514 (2010).
21. T. Okuhara, *Chem. Rev.* **102**, 3641–3666 (2002).
22. C. Bleschke, J. Schmidt, D. S. Kundu, S. Blechert A. Thomas, *Adv. Synth. Catal.* **353**, 3101–3106 (2011).
23. C. A. Wang *et al.*, *Chem. Eur. J.* **18**, 6718–6723 (2012).
24. C. E. Song, Ed., *Cinchona Alkaloids in Synthesis and Catalysis* (Wiley-VCH, Weinheim, Germany, 2009).
25. S. H. Oh *et al.*, *Angew. Chem. Int. Ed.* **47**, 7872–7875 (2008).
26. S. H. Youk *et al.*, *Chem. Commun.* **2009**, 2220–2222 (2009).
27. S. E. Park *et al.*, *Adv. Synth. Catal.* **352**, 2211–2217 (2010).
28. N. G. Anderson, *Org. Process Res. Dev.* **16**, 852–869 (2012).
29. L. B. Datsevich, in *Conventional Three-Phase Fixed-Bed Technologies*, L. B. Datsevich, Ed. (Springer, New York, 2012), pp. 7–9.
30. S. V. Ley *et al.*, *J. Chem. Soc. Perkin Trans. 1* **2000**, 3815–4195 (2000).

**Acknowledgments:** Generous support by Max Planck Society, DECHEMA (Gesellschaft für Chemische Technik und Biotechnologie e.V.), AIF (Arbeitsgemeinschaft Industrieller Forschungsvereinigungen “Otto von Guericke” e.V.)/IGF (Industrielle Gemeinschaftsforschung) 436 ZN, the Ministry of Education (Priority Research Centers Program, Republic of Korea), and the European Research Council (Advanced Grant “High Performance Lewis Acid Organocatalysis, HIPOCAT”) are gratefully acknowledged. We thank our analytical departments [mass spectroscopy, x-ray photoelectron spectroscopy (XPS analysis), nuclear magnetic resonance (NMR) spectroscopy, and high-performance liquid chromatography analysis] for excellent assistance. The authors have filed a patent on the methods presented herein.

**Supplementary Materials**

[www.sciencemag.org/cgi/content/full/341/6151/1225/DC1](http://www.sciencemag.org/cgi/content/full/341/6151/1225/DC1)

Materials and Methods

Supplementary Text

Figs. S1 to S8

Tables S1 to S8

Supplementary Data

References (31–38)

20 June 2013; accepted 5 August 2013

10.1126/science.1242196

# Slow Earthquakes, Preseismic Velocity Changes, and the Origin of Slow Frictional Stick-Slip

Bryan M. Kaproth and C. Marone

Earthquakes normally occur as frictional stick-slip instabilities, resulting in catastrophic failure and seismic rupture. Tectonic faults also fail in slow earthquakes with rupture durations of months or more, yet their origin is poorly understood. Here, we present laboratory observations of repetitive, slow stick-slip in serpentinite fault zones and mechanical evidence for their origin. We document a transition from unstable to stable frictional behavior with increasing slip velocity, providing a mechanism to limit the speed of slow earthquakes. We also document reduction of *P*-wave speed within the active shear zone before stick-slip events. If similar mechanisms operate in nature, our results suggest that higher-resolution studies of elastic properties in tectonic fault zones may aid in the search for reliable earthquake precursors.

Slow earthquakes represent one mode of the spectrum of fault slip behaviors ranging from steady aseismic slip at plate tectonic rates (a few millimeters per year) to normal earthquakes with rupture propagation at a few kilometers per second and fault slip speeds of 1 to 10 m/s, which is consistent with elastodynamic theory (1–6). Like normal earthquakes, slow earthquakes can accommodate most of a fault’s slip budget, with equivalent magnitudes of 8 or larger; yet, this slip occurs slowly, over days to years, rather than the few tens of seconds for normal earthquakes (1–4). Slow earthquakes often occur adjacent to traditional seismogenic zones (5, 7) and may load these earthquake-prone areas. Moreover, recent work suggests that slow earthquakes may abet potentially devastating earthquakes, such as the 2011  $M_w$  9 Tohoku Oki earthquake (7), and thus, understanding the physics of slow earthquakes and

identifying possible precursory changes in fault zone properties are increasingly important goals.

Although observations of slow earthquakes abound, the underlying processes that produce these self-sustaining, quasi-dynamic ruptures remain poorly understood (3–8). A particularly vexing aspect of slow earthquakes is the mechanism that limits slip speed yet allows self-sustained rupture propagation. One possibility is that slow earthquakes represent prematurely arrested normal earthquakes with slip-speed limited by a mechanism such as dilatant hardening or a transition in friction constitutive behavior with increasing slip speed. Several mechanisms have been proposed (4–12), but the origin of slow earthquakes remains elusive. Additionally, if slow earthquakes initiate like normal earthquakes they may exhibit precursory effects, such as accelerating fault slip or changes in elastic wave-speed within the rupture nucleation region.

Here, we describe laboratory observations of fault-zone materials showing repetitive, slow stick-slip friction events that are reminiscent of slow

earthquakes (Fig. 1). We sheared layers of lizardite-rich serpentinite at constant normal stress of 1 MPa (supplementary text). Each experiment includes 50+ stick-slip events, with durations ranging up to 35 s (Fig. 2). Our experiments show that the laboratory fault zones undergo a transition from velocity-weakening to velocity-strengthening friction behavior above slip rates of  $\sim 10$   $\mu\text{m/s}$  (Fig. 3). During each slip event, the fault zone shows large changes in elastic wave speed (2 to 21% decrease), with precursory changes of 1 to 3% starting up to 60 s before failure (Fig. 4).

Like natural earthquakes, fault slip velocity during stick-slip events exceeded the imposed far-field velocity. The full record for one experiment shows the character of stress drops and the corresponding stair-step pattern of fault displacement (Fig. 1A). Stick-slip events have durations of 1 to 35 s, average slip velocities of 15 to 280  $\mu\text{m/s}$ , average displacements of 10 to 900  $\mu\text{m}$ , and evolve from small to large events with increasing shear (Fig. 1B). We observed slow stick-slip events at a range of loading velocities (Fig. 2). Each event generally released tens of kilopascals of shear stress—roughly a 5 to 10% stress drop (Fig. 1A). Maximum slip velocities ranged from 60 to 1300  $\mu\text{m/s}$ , but peak velocities were generally sustained for  $<1$  s, with longer acceleration and deceleration periods (Fig. 2B). The events resemble results from experiments conducted on halite (12) but are distinguished by their consistent, repetitive nature.

To investigate the processes responsible for these slow-slip events, we conducted additional experiments under stiff loading conditions, including slide-hold-slide (SHS) (fig. S2) and velocity-step tests (fig. S3). We determined the friction rate parameter ( $a-b = \Delta\mu/\Delta\ln V$ , where  $V$  is the velocity) and critical slip distance ( $D_c$ ) using standard techniques (13). With increased shear strain and hold time, ( $a-b$ ) generally decreased, and  $D_c$  increased (fig. S2A). At slip velocities

Department of Geosciences, and Energy Institute Center for Geomechanics, Geofluids and Geohazards, Pennsylvania State University, University Park, PA 16802, USA.

of  $\leq 1 \mu\text{m/s}$ , SHS tests yielded ( $b$ - $a$ ) values of 0.2 to 0.002 (Fig. 3),  $D_c$  of 5 to 105  $\mu\text{m}$ , and thus values of the critical stiffness from 2.1 to 11.4 kN/mm, which exceeded the elastic stiffness of the loading system (fig. S2A). These ( $b$ - $a$ ) values are large compared with typical values for other materials (13–15). At higher velocities (3 to 1000  $\mu\text{m/s}$ ), velocity-step tests indicate ( $a$ - $b$ ) from  $-0.004$  to  $+0.018$ . Taken together, Fig. 3 shows that lizardite-rich serpentinite transitions from velocity-weakening,  $-(a$ - $b)$ , to velocity-strengthening,  $+(a$ - $b)$ , frictional behavior above a threshold velocity of  $\sim 10 \mu\text{m/s}$  (Fig. 3 and fig. S3). Previous works on lizardite at slip velocities  $\leq 10 \mu\text{m/s}$  show primarily velocity-weakening friction (14, 15), which is consistent with our results. At higher normal stress, lizardite continues to show velocity weakening above 10  $\mu\text{m/s}$  (14, 15), which may indicate that the transition from  $-(a$ - $b)$  to  $+(a$ - $b)$  with slip speed only occurs at low effective stresses. A similar

transition has been documented for halite (12), which was attributed to changes in asperity contact geometry and shear fabric. The frictional properties of lizardite serpentinite are distinct from antigorite and chrysotile serpentinite (14–17), which exhibit  $+(a$ - $b)$  at low velocities and transition to  $-(a$ - $b)$  at velocities above  $\sim 0.1 \mu\text{m/s}$  (15, 16), with dramatic weakening at higher slip rates (17).

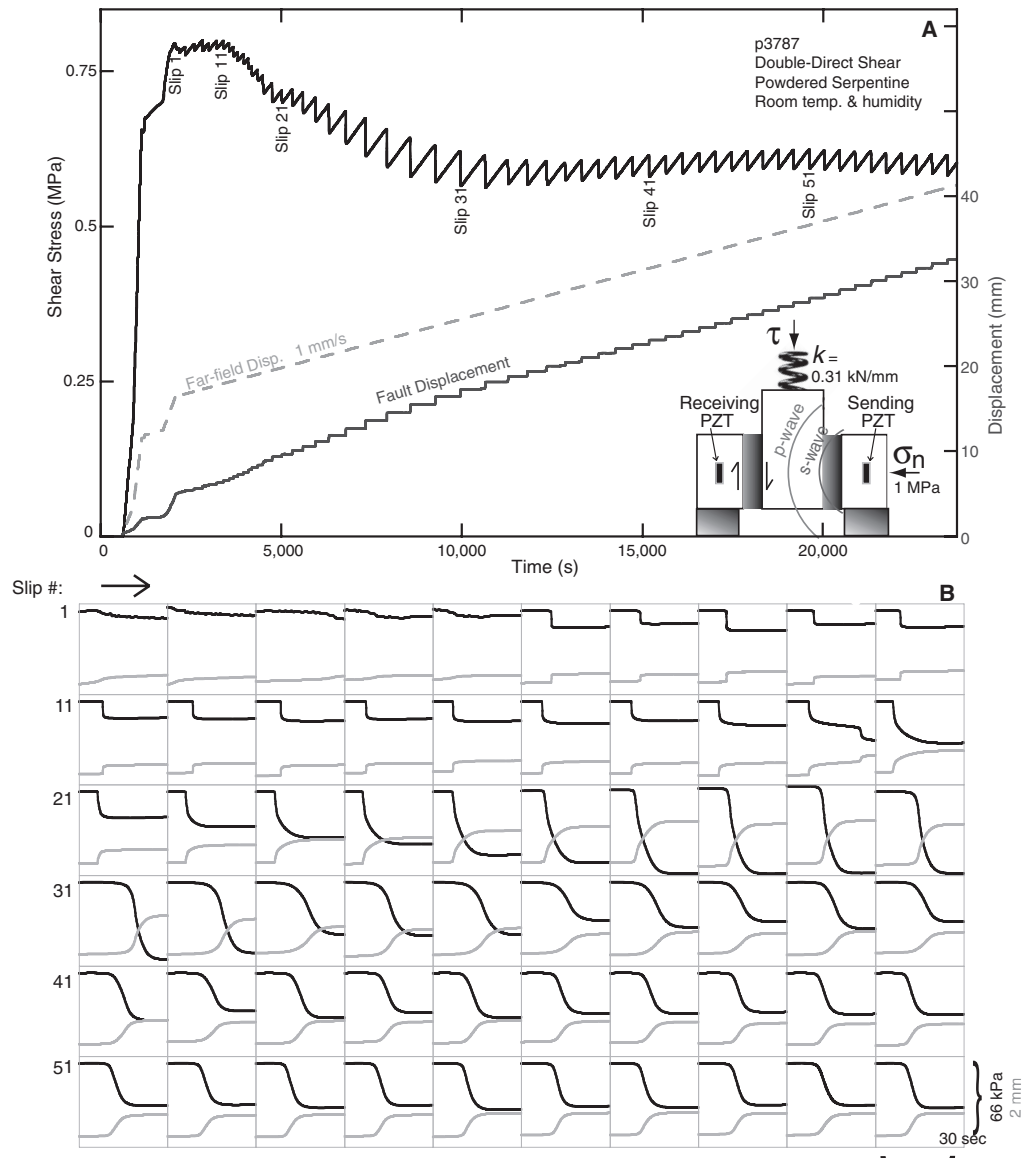
Our experiments included elastic wave-speed measurements, in which  $P$ -wave flight time increased during stick-slip events, with precursory excursions starting up to 60 s before failure (Fig. 4). Changes in  $P$ -wave flight time ( $T_{fl}$ ) for a complete experiment, determined from early  $P$ -wave coda, are shown in Fig. 4A along with the fault layer thickness and shear stress. The detailed flight time changes for each stick-slip event (Fig. 4B) are superimposed on long-term trends (Fig. 4A) derived from factors such as changes in grain contact stiffness and coordination number,

shear fabric development, and layer thinning (13, 18, 19). Correlation coefficients and pick fidelity decreased late in the experiment (Fig. 4A) because of increased sample attenuation (fig. S1).

Nine stick-slip events highlight  $T_{fl}$  changes before each event (Fig. 4B, inset), measured from peak stress. With up to  $\sim 0.2 \mu\text{s}$  flight time increase, absolute  $P$ -wave velocity ( $V_P$ ) of the fault layers decreased by 2 to 21% during these events (Fig. 4B). After each slip event,  $T_{fl}$  recovered with log time, and in many cases, the original flight time was recovered within 100 s (Fig. 4C). Before failure,  $T_{fl}$  increased by up to 0.06  $\mu\text{s}$ , accounting for 10 to 25% of the total  $V_P$  change during failure (Fig. 4B). These preseismic flight time changes occurred in tandem with, and were perhaps driven by, ultra-slow preseismic slip (fig. S4).

Our measurements indicate that serpentinite exhibits the necessary and sufficient conditions for dynamic earthquake rupture:  $-(a$ - $b)$  and  $k < k_c$  (Fig. 3 and figs. S2 and S3). Friction theory in-

**Fig. 1. A full experiment showing repetitive, slow stick-slip.** (A) Shear stress ( $\tau$ ; top solid line) during repeating stick-slip failure of serpentinite gouge under constant far-field velocity (dashed line). Like earthquake cycles,  $\tau$  builds over long periods but is released in punctuated slip events, creating steps in fault slip displacement. (Inset) The double-direct shear arrangement with the piezoelectric transducers (PZT). (B) Subplots show 30-s windows for each stick-slip event in (A), with event durations from 1 to 30 s. Fault slip (gray lines) is driven by stress release (black lines). There is a clear progression from small impulsive events to large slow events with increasing net displacement.



dicates that stick-slip initiates when shear stress ( $\tau$ ) exceeds fault strength and the rate of friction weakening exceeds the elastic unloading stiffness. To generate a large, dynamic earthquake rupture, the conditions for instability must persist as slip accelerates and the rupture expands. This requires fault weakening as slip velocity increases, which we observed at low slip velocities (Fig. 3). At higher velocities, serpentinite transitions to velocity-strengthening behavior (Fig. 3 and fig. S3), which causes deceleration and limits fault slip velocity

**Fig. 2. Stick-slip duration and fault displacement.** (A and B) Repetitive slow stick-slip occurred over a range of driving velocities in three experiments under otherwise identical conditions (circles, p3787, 1  $\mu\text{m/s}$ ; inverted triangles, p3786, 30  $\mu\text{m/s}$ ; triangles, p3983, 0.5  $\mu\text{m/s}$ ). Average slip velocities ( $V_a$ ) ranged from  $\sim 15$  to 280  $\mu\text{m/s}$ , with  $\sim 15$  to 50  $\mu\text{m/s}$  at slower driving velocities. (B) Details of slip acceleration history for representative stick-slip events. Maximum slip velocities ( $V_m$ ) ranged from 60 to 1100  $\mu\text{m/s}$ , but the fastest velocities were only sustained for short periods ( $< 1$  s). Acceleration and deceleration periods often lasted 10+ s, resulting in low average velocities.

(Fig. 3, inset). During stick-slip events, slip arrests after  $\tau$  becomes smaller than fault strength. Thus, larger ( $b-a$ ) values yield larger stress drops, perhaps explaining the large events at higher strains (Figs. 1 and 3).

Although these experiments do not include the full range of seismogenic conditions and fault zone fluid chemistry (13, 15), they indicate that slow earthquakes could result from the rate-dependent frictional behavior of the fault gouge itself (3, 9). Unlike previous examples of slow

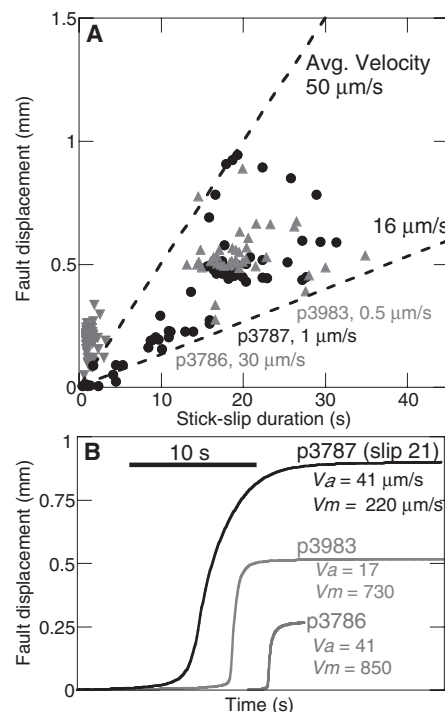
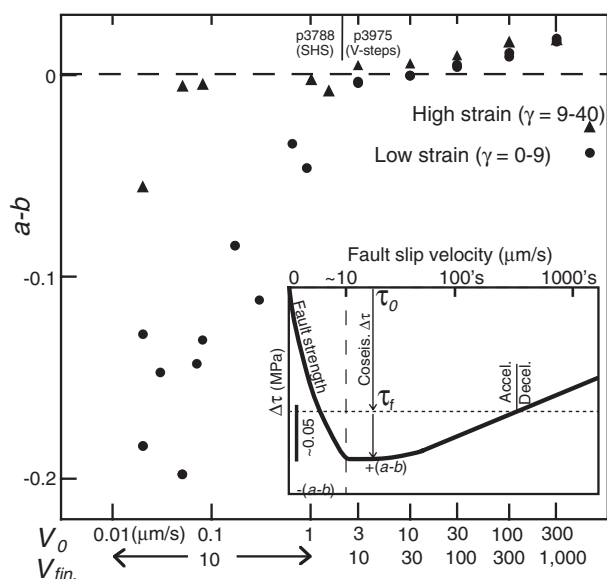


**Fig. 3. Frictional strength of serpentinite with fault slip speed.** Velocity weakening,  $-(a-b)$ , occurs at low velocities ( $\leq 10 \mu\text{m/s}$ ), which is a necessary condition for earthquake initiation.

At higher velocities, lizardite-rich serpentinite becomes velocity-strengthening, which would retard unstable slip. These ( $a-b$ ) values were determined from SHS tests (fig. S2) and velocity stepping tests (V-steps) (fig. S3), with initial ( $V_0$ ) and final ( $V_{fin}$ ) imposed slip velocities shown on the x axis. (Inset) A theoretical model for coseismic slip history. Fault slip begins when shear stress ( $\tau_0$ ) exceeds fault strength and accelerates until shear stress drops below fault strength. The observed transition in friction rate dependence means that fault slip decelerates above a threshold velocity. With continued coseismic stress release, slip velocity decreases to balance  $\tau$  and fault strength, causing slow deceleration and rupture arrest.



laboratory stick-slip with long durations (12), the mechanism we document is not limited to a specific fault stiffness and thus may be applicable to a wide range of fault conditions. Our results do not preclude other mechanisms for slow slip (such as dilatant hardening, dehydration reactions, slip weakening, and limited unstable fault area) (4–12). Our results are consistent with the observation that slow earthquake slip can occur over a range of fault velocities (4), suggesting the existence of a spectrum of seismic moment-release rates, dictated primarily by the transition between velocity-weakening and velocity-strengthening friction (Fig. 3) modulated by fault zone conditions.

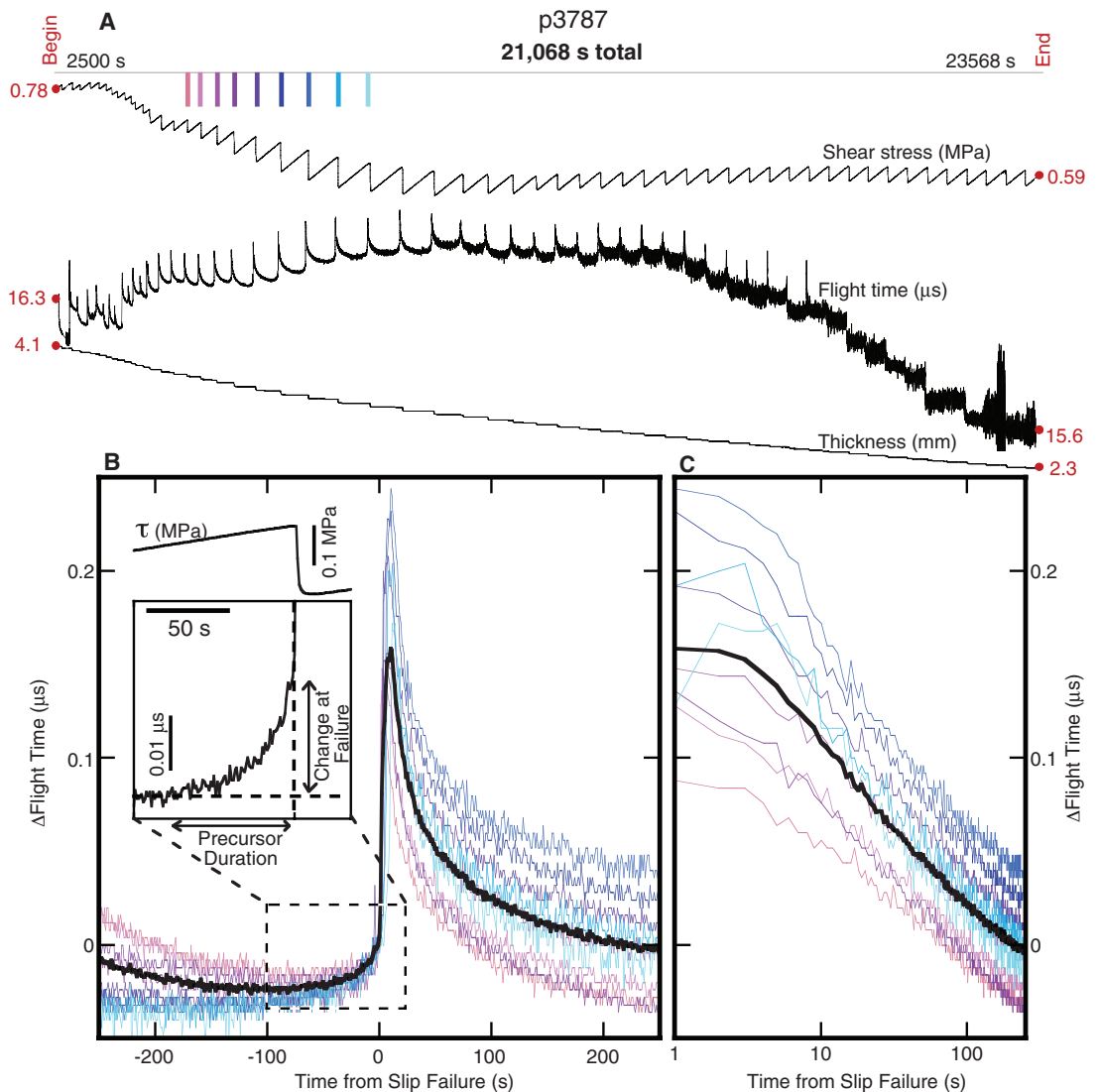
Existing studies of rupture nucleation (21, 22) show that variations in initial stress and fault strength can cause a range of dynamic rupture propagation rates and nucleation times (23). Our observations of slow slip provide an additional mechanism for slow rupture propagation, one that can also account for reproducible, periodic events.

Earthquakes involve fracturing and frictional failure, which commonly affect the elastic properties within the fault zone and surrounding rock (24, 25). Friction data and instability theory indicate that quasi-static slip within the fault zone should initiate before earthquake nucleation (26). One expects that this preseismic deformation will produce changes in fault properties such as elastic wave speed; however, there are few reliable observations of precursory changes before earthquake rupture (24). If most elastic changes occur within and directly adjacent to the fault zone, fault zone proximity may be a key limitation for many past, regionally focused studies (25).

Niu *et al.* (28) studied elastic wave speeds immediately adjacent to the San Andreas Fault and observed coseismic changes with apparent precursors (24). Our study also benefits from close fault proximity, and we observed large  $V_P$  changes (up to 20%), along with precursors that account for 10 to 25% of these changes starting up to 60 s before failure (Fig. 4). After failure, elastic velocity recovers with log time (Fig. 4C), which is consistent with field observations (25) and extensive laboratory studies of frictional healing (6, 13, 27). Precursory  $V_P$  changes are most likely tied to preseismic slip and nucleation of instability, as indicated by precise measurements of fault slip (fig. S4). Initial slip likely reduces  $V_P$  by a combination of dilation, damage to grain contacts, and grain fracture (18, 24–29). Our observations of elastic wave speed are consistent with granular dilation during stick-slip and associated changes in stress state, grain coordination number, and grain contact quality (18, 28–30), which evolve with shear deformation (19). These observations suggest that a renewed focus on field studies of temporal variations in elastic wave speed may be warranted in regions of high seismic hazard and that a combination of slow slip monitoring and elastic wave speed measurement may provide a basis for reliable earthquake prediction in regions where damaging, normal earthquakes are triggered by slow fault slip.

### Fig. 4. Preseismic and coseismic elastic wave-speed decrease and postseismic healing.

(A) Shear stress, fault thickness, and  $T_{fl}$  throughout experiment p3787. With each slip event,  $T_{fl}$  increases and gradually recovers. (B) Highlights of nine sequential events [identified by color dashes in (A)] chosen for low noise and long recurrence intervals. We stacked these events (black line) so as to enhance signal over noise. After peak stress,  $T_{fl}$  changes were large, accounting for changes in  $V_p$  of up to 2 to 21%; however, 10 to 25% of this decrease occurred before failure. Velocity changes preceded the main shear failure by up to 60 s (inset). (C) After each slip event,  $T_{fl}$  recovered with log time, indicating fault-healing after rupture (1, 13, 20, 23); 75% of baseline velocity was generally recovered after  $\sim 100$  s.



#### References and Notes

- I. Sacks, A. Linde, S. Suyehiro, J. Snoke, *Nature* **275**, 599–602 (1978).
- G. Dragert, K. Wang, T. S. James, *Science* **292**, 1525–1528 (2001).
- S. Ide, G. C. Beroza, D. R. Shelly, T. Uchide, *Nature* **447**, 76–79 (2007).
- Z. Peng, J. Gomberg, *Nat. Geosci.* **3**, 599–607 (2010).
- A. Ghosh, J. E. Vidale, K. C. Creager, *J. Geophys. Res.* **117**, B10301 (2012).
- C. Scholz, P. Molnar, T. Johnson, *J. Geophys. Res.* **77**, 6392–6406 (1972).
- A. Kato *et al.*, *Science* **335**, 705–708 (2012).
- M. Roy, C. Marone, *J. Geophys. Res.* **101**, 13919–13932 (1996).
- A. M. Rubin, *J. Geophys. Res.* **113**, B11414 (2008).
- M. J. Ikari, C. Marone, D. M. Saffer, A. J. Kopf, *Nat. Geosci.* **6**, 468–472 (2013).
- N. Brantut, J. Sulem, A. Schubnel, *J. Geophys. Res.* **116**, B05304 (2011).
- C. Voisin, J.-R. Grasso, E. Larose, F. Renard, *Geophys. Res. Lett.* **35**, L08302 (2008).
- C. Marone, *Annu. Rev. Earth Planet. Sci.* **26**, 643–696 (1998).
- M. Ikari, C. Marone, D. Saffer, *Geology* **39**, 83–86 (2011).
- D. E. Moore, D. A. Lockner, M. Shengli, R. Summers, J. D. Byerlee, *J. Geophys. Res.* **102**, 14787–14801 (1997).
- L. A. Reinen, J. D. Weeks, T. E. Tullis, *Pure Appl. Geophys.* **143**, 317–358 (1994).
- A. H. Kohli, D. L. Goldsby, G. Hirth, T. Tullis, *J. Geophys. Res.* **116**, B03202 (2011).
- M. W. Knuth, H. J. Tobin, C. Marone, *Granul. Matter*; published online May 2013.
- S. H. Haines, B. M. Kaproth, C. Marone, D. Saffer, B. A. van der Pluijm, *J. Struct. Geol.* **51**, 206–225 (2013).
- C. H. Scholz, *The Mechanics of Earthquakes and Faulting* (Cambridge Univ. Press, Cambridge, ed. 2, 2002), pp. 81–97.
- O. Ben-David, S. M. Rubinstein, J. Fineberg, *Nature* **463**, 76–79 (2010).
- A. Schubnel, S. Nielsen, J. Taddeucci, S. Vinciguerra, S. Rao, *Earth Planet. Sci. Lett.* **308**, 424–432 (2011).
- W. L. Ellsworth, G. C. Beroza, *Science* **268**, 851–855 (1995).
- F. Niu, P. G. Silver, T. M. Daley, X. Cheng, E. L. Majer, *Nature* **454**, 204–208 (2008).
- D. Rivet *et al.*, *Geophys. Res. Lett.* **38**, L08308 (2011).
- M. Bouchon, V. Durand, D. Marsan, H. Karabulut, J. Schmittbuhl, *Nat. Geosci.* **6**, 299–302 (2013).
- J. H. Dieterich, B. D. Kilgore, *Pure Appl. Geophys.* **143**, 283–302 (1994).
- J. Fortin, Y. Guéguen, A. Schubnel, *J. Geophys. Res.* **112**, (B8), B08207 (2007).
- J. D. Goddard, *Proc. Soc. R., Math. Phys. Eng. Sci.* **430**, 105–131 (1990).
- A. Schubnel, B. D. Thompson, J. Fortin, Y. Guéguen, R. P. Young, *Geophys. Res. Lett.* **34**, L19307 (2007).

**Acknowledgments:** We thank B. Carpenter, M. Scuderi, J. Leeman, M. Ikari, and S. Swavelly for assistance in the laboratory and S. Haines and D. Moore for their help with x-ray diffraction interpretation. This work was supported by NSF grants OCE-0648331, EAR-0746192, and EAR-0950517. Data are available in the supplementary materials.

#### Supplementary Materials

[www.sciencemag.org/cgi/content/full/science.1239577/DC1](http://www.sciencemag.org/cgi/content/full/science.1239577/DC1)  
Materials and Methods  
Supplementary Text  
Figs. S1 to S4  
References  
Supplementary Data Files

24 April 2013; accepted 1 August 2013  
Published online 15 August 2013;  
10.1126/science.1239577



[www.sciencemag.org/cgi/content/full/science.1239577/DC1](http://www.sciencemag.org/cgi/content/full/science.1239577/DC1)

## Supplementary Material for

### **Slow Earthquakes, Preseismic Velocity Changes, and the Origin of Slow Frictional Stick-Slip**

Bryan M. Kaproth and C. Marone

Published 15 August 2013 on *Science Express*  
DOI: 10.1126/science.1239577

**This PDF file includes:**

Materials and Methods

Supplementary Text

Figs. S1 to S4

References

**Other Supplementary Material for this manuscript includes the following:**

(available at [www.sciencemag.org/cgi/content/full/science.1239577/DC1](http://www.sciencemag.org/cgi/content/full/science.1239577/DC1))

Supplementary Data Files as zipped archives: p3787\_data.txt, p3787\_data\_raw.txt, p3787\_seismograms.txt, p3786\_data.txt, p3786\_seismograms.txt, p3983\_data.txt

## Materials and Methods

### Friction experiment details and materials

These experiments were conducted in a biaxial forcing apparatus under double-direct shear (13). Our configuration consisted of two fault zones sandwiched between three steel forcing blocks (Fig. 1A, inset), with normal stress applied horizontally and shear stress applied vertically. Fast acting servo-hydraulic controllers maintain specified conditions of constant horizontal force and constant vertical displacement rate. We measured force using strain gauge load cells, accurate to +/- 0.1 kPa for our sample dimensions (5 cm x 5 cm frictional contact area), and displacement (layer thickness in the horizontal direction and shear displacement in the vertical direction) using direct current displacement transducers, accurate to +/- 0.1  $\mu\text{m}$ . Stresses and displacements were recorded digitally at 10 kHz with a 24 bit system, and were averaged to 10-100 Hz for storage. To promote stick-slip failure we reduced the shear-loading stiffness with an elastic element ( $k = 0.31 \text{ kN/mm}$ ; Fig. 1A, inset) in the main set of experiments.

We sheared layers of synthetic fault gouge composed of serpentinite (Eden Mills, VT) purchased from Wards as rock fragments. XRD analysis shows that this serpentinite is primarily lizardite with some antigorite, and that it contains <3% chlorite and pumpellyite. We powdered the serpentinite rock in a rotary mill until all particles passed through a 106  $\mu\text{m}$  sieve. Layers were constructed from this powder.

Experiments were carried out on powdered serpentinite, with 3 mm initial layer thickness, and at room temperature and humidity (>75% RH). Normal stress was held constant at 1 MPa, plausibly appropriate for slow earthquakes in nature (1). We conducted three types of experiments. (1) Stick-slip experiments were carried out with a spring in the vertical axis to reduce the system stiffness. Sliding velocity for these experiments was held constant in the range 0.5 to 30  $\mu\text{m/s}$ , with faster velocities used during initial loading (Fig. 1A). (2) The slide-hold-slide experiment (p3788) was conducted under stiff loading conditions (i.e. no spring). In total, three slide-hold-slide sequences were conducted as follows: shear 1 mm, 1 s hold, shear 1 mm, 3 s hold, shear 1 mm, 10 s hold, shear 1.5 mm, 30 s hold, shear 1.5 mm, 100 s hold, shear 1.5 mm. All shear was conducted at 10  $\mu\text{m/s}$  shear loading velocity. The first, second, and third slide-hold-slide sequences were started at 3, 19, and 26 mm of net shear displacement, respectively. Each slide-hold-slide sequence was modeled using the Ruina rate/state friction law to determine best-fit frictional constitutive properties (i.e.  $(a-b)$ ,  $D_c$ ,  $k_c$ ). (3) The velocity-stepping experiment (p3975) was also conducted under stiff loading conditions. In total, three velocity-stepping sequences were conducted as follows: 0.4 mm of shear in sequence from 10  $\mu\text{m/s}$ , 3  $\mu\text{m/s}$ , 10  $\mu\text{m/s}$ , 30  $\mu\text{m/s}$ , 100  $\mu\text{m/s}$ , 300  $\mu\text{m/s}$ , and 1,000  $\mu\text{m/s}$ . The first, second, and third velocity-stepping sequence were started at 2, 16, 25 mm of net shear displacement, respectively. Velocity steps were modeled using the Ruina rate and state friction law (13) coupled with elastic interaction of the testing machine.

## Ultrasonic measurements

Elastic properties were measured with two, 0.5", Lithium Niobate, dual mode piezoelectric transducers (PZT) purchased from Boston Piezo Optics and installed in the side forcing blocks of the double direct shear assembly with Faraday cages. These transducers generate 1,400 kHz and 900 kHz P- and S-waves, respectively. We excited one PZT (Fig. 1) with a 900 V pulse with 0.1-4  $\mu$ s pulse width and a 20 Hz repetition rate generated by an Olympus NDT Model 5058PR pulser-receiver. At this voltage, the transducer generates a  $\sim$  19 nm and  $\sim$  1 nm amplitude P- and S-wave, respectively (compressional wave piezoelectric constant = 20.8 pm/V; shear wave piezoelectric constant = 0.8 pm/V). An identical transducer in the opposite side block received the waveforms (Fig. 1). We recorded the output response with a GaGe CS8382 multi-channel digitizer at 25 MHz (14 bit over a 1 V range). We focused primarily on P-waves throughout these experiments, because S-waves were emergent relative to the strong P-wave coda (Fig. S1). The signal to noise ratio was enhanced by (1) using a very large excitation voltage, (2) stacking the waveforms (generally 20 per seismogram), and (3) shielding the transducers with Faraday cages.

We picked the P-wave and P-coda arrivals via cross correlation. We used standard seismic techniques wherein a master waveform was compared to recorded seismograms for a range of time offsets to identify a shift in the wave flight time, or the time for the wave to go from the pulser to the receiving transducer (Fig. 1A, inset). After selecting a master wave with high signal to noise ratio, we compared it against a moving window for every other seismogram, and made a pick at the highest correlation coefficient. One benefit of cross correlation is that it can offer up to a tenfold resolution increase compared to the data sampling rate. Thus, we subsampled each master wave and seismogram with a 10x spline fit.

We calculated the absolute P-wave velocity throughout each experiment, following  $V_p = h/(T_p - T_p^0)$ , where  $h$  is the layer thickness,  $T_p$  is the P-wave flight time and  $T_p^0$  is the P-wave flight time from calibrations with no gouge layer. The calibration was carried out repeatedly to verify results:  $T_p^0 = 11.36 \mu$ s. P-wave arrivals were noisy and thus we focused on velocity changes indicated by the P-wave coda. In general, the coda lagged behind the P-wave arrival with remarkable consistency (Fig. 1B), following it by  $\sim$  2.4  $\mu$ s. Therefore this term was used to obtain changes in absolute value of the P-wave velocity.

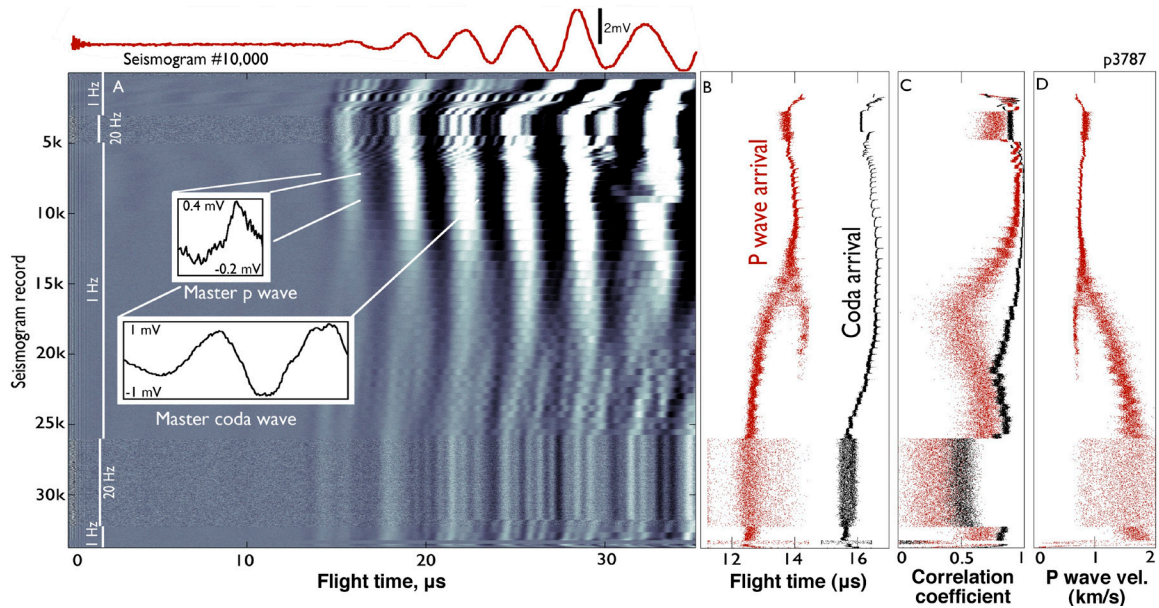


**Fig. S1.** (A) Over the course of one experiment, we collected 30,000+ waveforms. These seismograms are shown sequentially in panel A, with the earliest at the top and latest at bottom. An example seismogram (record 10,000) is shown above this plot; note the emergent P-wave arrival around 14  $\mu\text{s}$ . To measure the P-wave arrival (B), we cross-correlated each waveform throughout the experiment (panel C shows correlation coefficients) against a master waveform (A, smaller inset). We determined  $V_p$  throughout the experiment (D) using layer thickness measurements and  $T_{fl}$ , with calibrations for the flight time through the forcing blocks. Because the P-wave was emergent, we also cross-correlated two cycles of coda (A, larger inset), starting one cycle after the P-wave arrival. In general, the overall trends of the P-wave arrival and coda were similar, but the coda had much less noise (B), reflected in the correlation coefficients (C). For most of this experiment, we collected one seismogram per second (stacking 20 records). However, we collected unstacked seismograms at much higher rates (20 Hz) over two periods (see white line at left side of A). While these periods gave higher sampling resolution, the arrival picks (B) are noisier, owing to increased seismogram noise without a stack. Additionally, the seismic signal got very weak after record  $\sim 12,000$ , increasing the flight time noise, likely owing to increased attenuation within the fault layers.

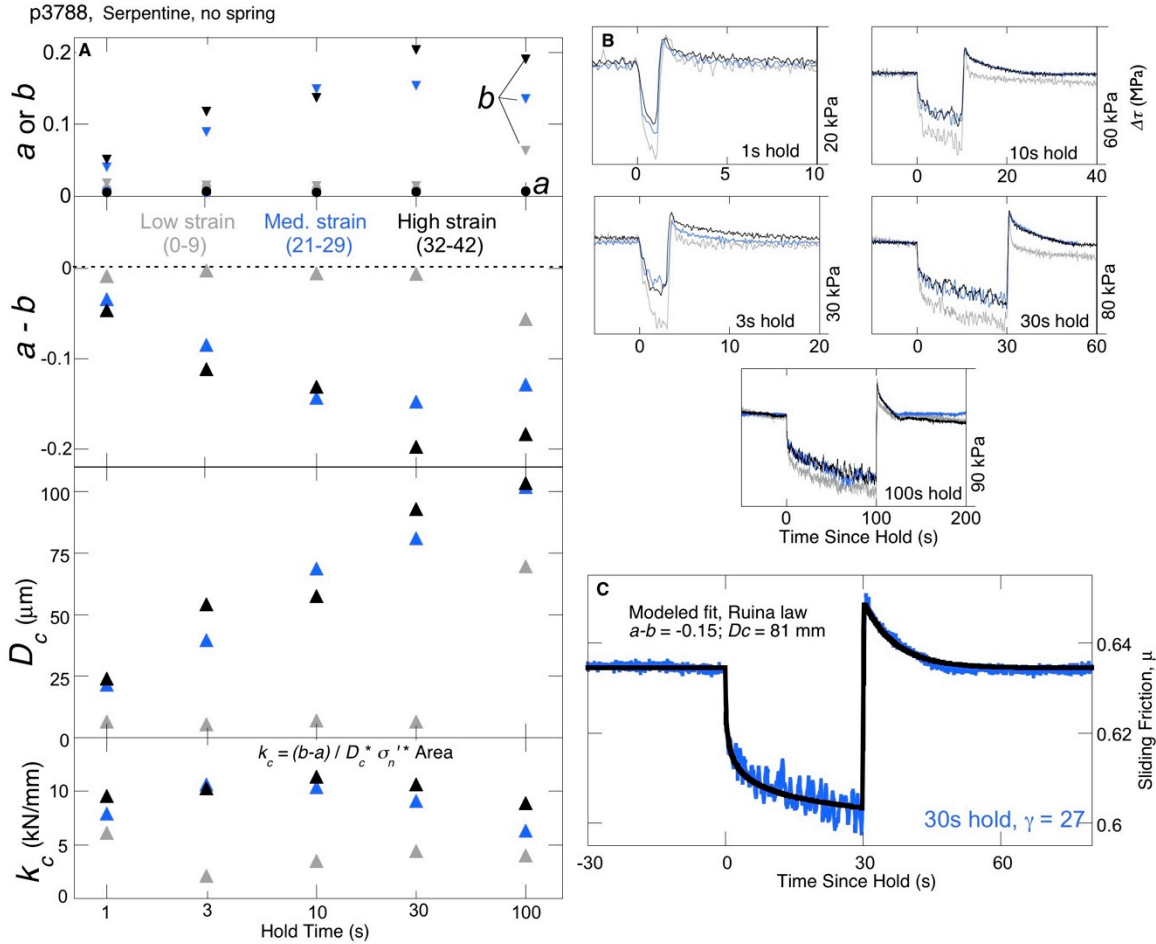


**Fig. S2.** Results of the rate/state friction modeling (A) along with details of the data (B, C) showing how parameters were obtained. We conducted slide-hold-slide tests in a stiff system to determine the frictional properties of serpentine. During this experiment five hold periods (1-100 s) were conducted at low, medium, and high strain, each followed by 1.0 to 1.5 mm of shear at  $10 \mu\text{m/s}$ . All other variables were held constant (room temp and humidity,  $\sigma_n = 1 \text{ MPa}$ ). Examples of data from the slide-hold-slide sequences are shown in (B). We modeled each sequence (Panel C) to determine  $a$  (circles),  $b$  (upside down triangles),  $(a-b)$ ,  $D_c$ , and  $k_c$ , as a function of hold time and strain (A). Under all conditions, serpentine was velocity weakening,  $-(a-b)$ , satisfying the necessary condition for earthquake slip. At low strains,  $(a-b)$  and  $D_c$  were roughly independent of hold time. At all other strains,  $(b-a)$  and  $D_c$  were large, and tended to increase with hold time. Changes in  $(b-a)$  were generally controlled by  $b$  (0.01-0.2), as  $a$  was consistently less than 0.01. The critical stiffness ranged from 2 to 11  $\text{kN/mm}$  and tended to be larger at higher strains. The measured values of  $k_c$  are higher than the elastic loading stiffness (0.31  $\text{kN/mm}$ ), and thus the sufficient condition for friction instability, to first order, was met at low velocity.

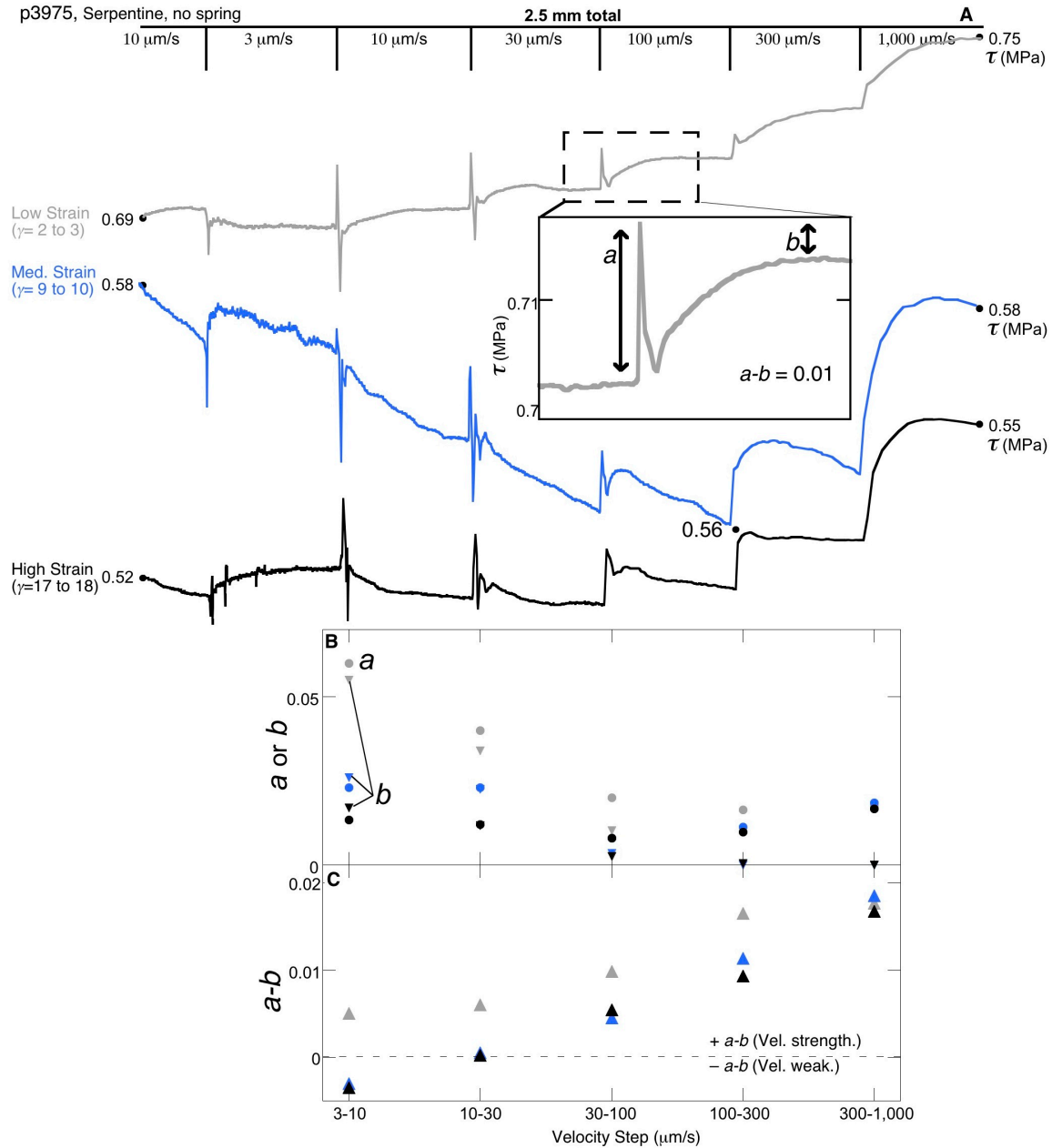


**Fig. S3.** Friction data for velocity step tests in an experiment performed under stiff loading conditions to determine rate/state constitutive parameters at velocities (from 3 to  $1,000 \mu\text{m/s}$ ). Inset illustrates the friction parameters  $a$  and  $b$ . Conditions for this experiment were similar to the slow stick-slip experiments (room temp, 100% humidity,  $\sigma_n = 1 \text{ MPa}$ ). Panel A highlights shear stress during three velocity stepping sequences at low (gray line), medium (blue line), and high (black line) strain. Each sequence shows step changes in loading velocity, separated by  $0.4 \mu\text{m}$  of shear, from 3, 10, 30, 100, 300 and  $1,000 \mu\text{m/s}$ , starting from an initial velocity of  $10 \mu\text{m/s}$ . We estimated  $a$  (circles) and  $b$  (upside down triangles) for each velocity step (B) accounting for elastic interaction of the testing machine and using forward models of the Ruina rate and state friction law. In general,  $(a-b)$  increased with velocity, and decreased with strain (C). At higher strain ( $\gamma = 9-10$  and  $\gamma = 17-18$ ), serpentine was velocity weakening below slip rates of  $\sim 10 \mu\text{m/s}$ .

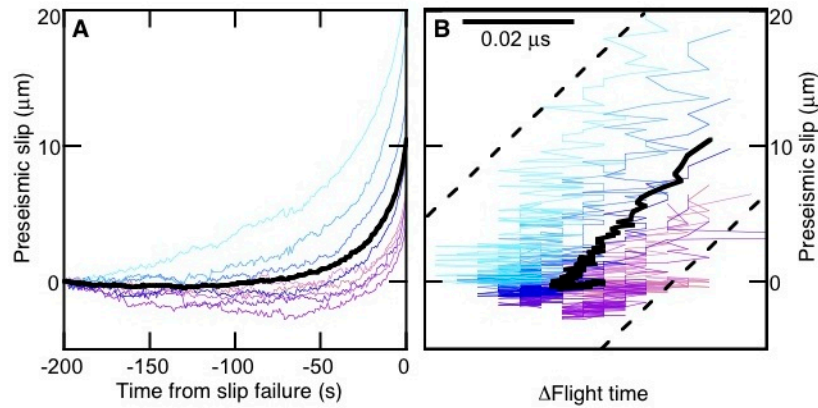


**Fig. S4.** (A) Before each stick-slip event, the fault zone accommodates small amounts of slip ( $< 20 \mu\text{m}$ ). (B) Within 60 seconds before failure,  $T_{fl}$  increases proportionately with preseismic slip. Preseismic slip may cause  $V_p$  changes by shear driven dilation or damage to well-healed grain contacts, and similar processes may drive precursor velocity changes in nature (9, 21, 23).

Supplementary data files for manuscript #1239577

**p3787\_data.txt:** This data file contains decimated experiment data from experiment p3787. Each row of data corresponds to a seismogram of the same row number in p3787\_seismograms.txt. Columns 1-8 contain: (1) vertical load point displacement,  $\mu\text{m}$ , (2) shear stress, MPa, (3) total gouge layer thickness,  $\mu\text{m}$ , (4) normal stress, MPa, (5) time, seconds, (6) coefficient of sliding friction, (7) shear strain, (8) shear displacement corrected for spring stiffness,  $\mu\text{m}$ .

**p3787\_data\_raw.txt:** This data file contains all friction data for p3787 without decimation (this file does not correspond with p3787\_seismograms.txt). Columns 1-8 contain: (1) vertical load point displacement,  $\mu\text{m}$ , (2) shear stress, MPa, (3) total gouge layer thickness,  $\mu\text{m}$ , (4) normal stress, MPa, (5) time, seconds, (6) coefficient of sliding friction, (7) shear strain, (8) shear displacement corrected for spring stiffness,  $\mu\text{m}$ .

**p3787\_seismograms.txt:** This data file contains all seismograms for experiment p3787. Each row is a seismogram corresponding to the same row of data in p3787\_data.txt. For a given seismogram, a datapoint is recorded every  $0.04 \mu\text{s}$  (e.g., datapoint 200 corresponds to  $8 \mu\text{s}$  since the excitation of the transmitting PZT), with amplitude reported in mV. Most seismograms represent a stack of 20 waveforms (see Fig. S1).

**p3786\_data.txt:** This data file contains decimated experiment data from experiment p3786. Each row of data corresponds to a seismogram of the same row number in p3786\_seismograms.txt. Columns 1-8 contain: (1) vertical load point displacement,  $\mu\text{m}$ , (2) shear stress, MPa, (3) total gouge layer thickness,  $\mu\text{m}$ , (4) normal stress, MPa, (5) time, seconds, (6) coefficient of sliding friction, (7) shear strain, (8) shear displacement corrected for spring stiffness,  $\mu\text{m}$ .

**p3786\_seismograms.txt:** This data file contains all seismograms for experiment p3786. Each row is a seismogram corresponding to the same row of data in p3786\_data.txt. For a given seismogram, a datapoint is recorded every  $0.04 \mu\text{s}$  (e.g., datapoint 200 corresponds to  $8 \mu\text{s}$  since the excitation of the transmitting PZT), with amplitude reported in mV. Most seismograms represent a stack of 20 waveforms.

**p3983\_data.txt:** This data file contains decimated experiment data from experiment p3983. Columns 1-8 contain: (1) vertical load point displacement,  $\mu\text{m}$ , (2) shear stress, MPa, (3) total gouge layer thickness,  $\mu\text{m}$ , (4) normal stress, MPa, (5) time, seconds, (6) coefficient of sliding friction, (7) shear strain, (8) shear displacement corrected for spring stiffness,  $\mu\text{m}$ .

## References and Notes

1. I. Sacks, A. Linde, S. Suyehiro, J. Snoke, Slow earthquakes and stress redistribution. *Nature* **275**, 599–602 (1978). [doi:10.1038/275599a0](https://doi.org/10.1038/275599a0)
2. G. Dragert, K. Wang, T. S. James, A silent slip event on the deeper Cascadia subduction interface. *Science* **292**, 1525–1528 (2001). [doi:10.1126/science.1060152](https://doi.org/10.1126/science.1060152) [Medline](#)
3. S. Ide, G. C. Beroza, D. R. Shelly, T. Uchide, A scaling law for slow earthquakes. *Nature* **447**, 76–79 (2007). [doi:10.1038/nature05780](https://doi.org/10.1038/nature05780) [Medline](#)
4. Z. Peng, J. Gomberg, An integrated perspective of the continuum between earthquakes and slow-slip phenomena. *Nat. Geosci.* **3**, 599–607 (2010). [doi:10.1038/ngeo940](https://doi.org/10.1038/ngeo940)
5. A. Ghosh, J. E. Vidale, K. C. Creager, Tremor asperities in the transition zone control evolution of slow earthquakes. *J. Geophys. Res.* **117**, (B10), B10301 (2012). [doi:10.1029/2012JB009249](https://doi.org/10.1029/2012JB009249)
6. C. Scholz, P. Molnar, T. Johnson, Detailed studies of frictional sliding of granite and implications for the earthquake mechanism. *J. Geophys. Res.* **77**, 6392–6406 (1972). [doi:10.1029/JB077i032p06392](https://doi.org/10.1029/JB077i032p06392)
7. A. Kato, K. Obara, T. Igarashi, H. Tsuruoka, S. Nakagawa, N. Hirata, Propagation of slow slip leading up to the 2011 M(w) 9.0 Tohoku-Oki earthquake. *Science* **335**, 705–708 (2012). [doi:10.1126/science.1215141](https://doi.org/10.1126/science.1215141) [Medline](#)
8. M. Roy, C. Marone, Earthquake nucleation on model faults with rate- and state-dependent friction: Effects of inertia. *J. Geophys. Res.* **101**, (B6), 13919–13932 (1996). [doi:10.1029/96JB00529](https://doi.org/10.1029/96JB00529)
9. A. M. Rubin, Episodic slow slip events and rate-and-state friction. *J. Geophys. Res.* **113**, (B11), B11414 (2008). [doi:10.1029/2008JB005642](https://doi.org/10.1029/2008JB005642)
10. M. J. Ikari, C. Marone, D. M. Saffer, A. J. Kopf, Slip weakening as a mechanism for slow earthquakes. *Nat. Geosci.* **6**, 468–472 (2013). [doi:10.1038/ngeo1818](https://doi.org/10.1038/ngeo1818)
11. N. Brantut, J. Sulem, A. Schubnel, Effect of dehydration reactions on earthquake nucleation: Stable sliding, slow transients, and unstable slip. *J. Geophys. Res.* **116**, (B5), B05304 (2011). [doi:10.1029/2010JB007876](https://doi.org/10.1029/2010JB007876)
12. C. Voisin, J.-R. Grasso, E. Larose, F. Renard, Evolution of seismic signals and slip patterns along subduction zones: Insights from a friction lab scale experiment. *Geophys. Res. Lett.* **35**, L08302 (2008). [doi:10.1029/2008GL033356](https://doi.org/10.1029/2008GL033356)
13. C. Marone, Laboratory-derived friction laws and their application to seismic faulting. *Annu. Rev. Earth Planet. Sci.* **26**, 643–696 (1998). [doi:10.1146/annurev.earth.26.1.643](https://doi.org/10.1146/annurev.earth.26.1.643)
14. M. Ikari, C. Marone, D. Saffer, On the relation between fault strength and frictional stability. *Geology* **39**, 83–86 (2011). [doi:10.1130/G31416.1](https://doi.org/10.1130/G31416.1)
15. D. E. Moore, D. A. Lockner, M. Shengli, R. Summers, J. D. Byerlee, Strengths of serpentinite gouges at elevated temperatures. *J. Geophys. Res.* **102**, (B7), 14787–14801 (1997). [doi:10.1029/97JB00995](https://doi.org/10.1029/97JB00995)

16. L. A. Reinen, J. D. Weeks, T. E. Tullis, The frictional behavior of lizardite and antigorite serpentinites: Experiments, constitutive models, and implications for natural faults. *Pure Appl. Geophys.* **143**, 317–358 (1994).  
[doi:10.1007/BF00874334](https://doi.org/10.1007/BF00874334)
17. A. H. Kohli, D. L. Goldsby, G. Hirth, T. Tullis, Flash weakening of serpentinite at near-seismic slip rates. *J. Geophys. Res.* **116**, (B3), B03202 (2011).  
[doi:10.1029/2010JB007833](https://doi.org/10.1029/2010JB007833)
18. M. W. Knuth, H. J. Tobin, C. Marone, Evolution of ultrasonic velocity and dynamic elastic moduli with shear strain in granular layers. *Granul. Matter*. Published online May 2013. 10.1007/s10035-013-0420-1
19. S. H. Haines, B. M. Kaproth, C. Marone, D. Saffer, B. A. van der Pluijm, Shear zones in clay-rich fault gouge: A laboratory study of fabric element development and evolution. *J. Struct. Geol.* **51**, 206–225 (2013). [doi:10.1016/j.jsg.2013.01.002](https://doi.org/10.1016/j.jsg.2013.01.002)
20. C. H. Scholz, *The Mechanics of Earthquakes and Faulting* (Caimbridge University Press, Caimbridge, UK, ed. 2nd, 2002), pp. 81–97.
21. O. Ben-David, S. M. Rubinstein, J. Fineberg, Slip-stick and the evolution of frictional strength. *Nature* **463**, 76–79 (2010). [doi:10.1038/nature08676](https://doi.org/10.1038/nature08676) [Medline](#)
22. A. Schubnel, S. Nielsen, J. Taddeucci, S. Vinciguerra, S. Rao, Photo-acoustic study of subshear and supershear ruptures in the laboratory. *Earth Planet. Sci. Lett.* **308**, 424–432 (2011). [doi:10.1016/j.epsl.2011.06.013](https://doi.org/10.1016/j.epsl.2011.06.013)
23. W. L. Ellsworth, G. C. Beroza, Seismic evidence for an earthquake nucleation phase. *Science* **268**, 851–855 (1995). [doi:10.1126/science.268.5212.851](https://doi.org/10.1126/science.268.5212.851) [Medline](#)
24. F. Niu, P. G. Silver, T. M. Daley, X. Cheng, E. L. Majer, Preseismic velocity changes observed from active source monitoring at the Parkfield SAFOD drill site. *Nature* **454**, 204–208 (2008). [doi:10.1038/nature07111](https://doi.org/10.1038/nature07111) [Medline](#)
25. D. Rivet, M. Campillo, N. M. Shapiro, V. Cruz-Atienza, M. Radiguet, N. Cotte, V. Kostoglodov, Seismic evidence of nonlinear crustal deformation during a large slow slip event in Mexico. *Geophys. Res. Lett.* **38**, L08308 (2011).  
[doi:10.1029/2011GL047151](https://doi.org/10.1029/2011GL047151)
26. M. Bouchon, V. Durand, D. Marsan, H. Karabulut, J. Schmittbuhl, The long precursory phase of most large interplate earthquakes. *Nat. Geosci.* **6**, 299–302 (2013). [doi:10.1038/ngeo1770](https://doi.org/10.1038/ngeo1770)
27. J. H. Dieterich, B. D. Kilgore, Direct observation of frictional contacts: New insights for state-dependent properties. *Pure Appl. Geophys.* **143**, 283–302 (1994).  
[doi:10.1007/BF00874332](https://doi.org/10.1007/BF00874332)
28. J. Fortin, Y. Guéguen, A. Schubnel, Effects of pore collapse and grain crushing on ultrasonic velocities and  $V_p/V_s$ . *J. Geophys. Res.* **112**, (B8), B08207 (2007).  
[doi:10.1029/2005JB004005](https://doi.org/10.1029/2005JB004005)
29. J. D. Goddard, Nonlinear elasticity and pressure-dependent wave speeds in granular media. *Proc.- Royal Soc., Math. Phys. Eng. Sci.* **430**, 105–131 (1990).  
[doi:10.1098/rspa.1990.0083](https://doi.org/10.1098/rspa.1990.0083)

<jrn>30. A. Schubnel, B. D. Thompson, J. Fortin, Y. Guéguen, R. P. Young, Fluid-induced rupture experiment on Fontainebleau sandstone: Premonitory activity, rupture propagation, and aftershocks. *Geophys. Res. Lett.* **34**, L19307 (2007). [doi:10.1029/2007GL031076](https://doi.org/10.1029/2007GL031076)</jrn>